

Research Article

# MPS and MRI efficacy of magnetosomes from wild-type and mutant bacterial strains

David Heinke<sup>a,\*</sup> · Alexander Kraupner<sup>a</sup> · Dietmar Eberbeck<sup>b</sup> · Daniel Schmidt<sup>b</sup> · Patricia Radon<sup>b</sup> · René Uebe<sup>c</sup> · Dirk Schüler<sup>c</sup> · Andreas Briel<sup>a</sup>

<sup>a</sup>nanoPET Pharma GmbH, Berlin, Germany

<sup>b</sup>Physikalisch-Technische Bundesanstalt, Berlin, Germany

<sup>c</sup>University of Bayreuth, Bayreuth, Germany

\*Corresponding author, email: david.heinke@nanopet.de

Received 23 November 2016; Accepted 2 May 2017; Published online 22 June 2017

© 2017 Heinke; licensee Infinite Science Publishing GmbH

This is an Open Access article distributed under the terms of the Creative Commons Attribution License (<http://creativecommons.org/licenses/by/4.0>), which permits unrestricted use, distribution, and reproduction in any medium, provided the original work is properly cited.

## Abstract

The future of Magnetic Particle Imaging (MPI), as a tracer-based imaging modality, crucially relies on the development of high-performing tracers. Due to their ideal structural and magnetic properties, biogenic nanoparticles extracted from magnetotactic bacteria are promising candidates for MPI tracer research. In the present study we investigate the potential of bacterial magnetosomes, extracted from wild-type bacteria of the strain *Magnetospirillum gryphiswaldense* and various mutants thereof, as new tracer materials for MPI. Furthermore, we investigate the structural and magnetic properties of the magnetosomes as well as their suitability as Magnetic Resonance Imaging (MRI) agents in order to explain differences in MPI and MRI efficacies.

## 1. Introduction

Besides technological advancements of the Magnetic Particle Imaging (MPI) scanner and image reconstruction methods, the future of this tracer-based imaging technology crucially relies on the development of high-performing tracer materials. Due to their superior magnetic properties, iron oxide nanoparticles synthesized by magnetotactic bacteria constitute a potential tracer material [1]. These bacterial organisms conduct biomineralization, which is the process of formation of solid material within biological systems. The product of this biologically-controlled process are so-called magnetosomes, which serve as magnetic sensors for magnetotaxis, the orientation along the earth's magnetic field. These monocrystalline nanoparticles consist of pure and almost defect-free magnetite with fully matured particles having a high monodispersity in size and shape, while

their colloidal stability is maintained by biomembranes surrounding each particle [2]. Therefore, magnetosomes are promising candidates as high-performing tracers for MPI. Indeed, some of the highest MPI efficacies found so far were observed by Kraupner et al. for magnetite nanoparticles synthesized by magnetotactic bacteria of a mutant strain of *Magnetospirillum gryphiswaldense* [3]. Based on these results we investigate the potential of biogenic iron oxide nanoparticles extracted from wild-type *Magnetospirillum gryphiswaldense* strains and various other mutants thereof, as new tracer materials for MPI with a focus on the size dependency. We compare the results to those obtained with Resovist<sup>®</sup>, the former MRI gold-standard as well as standard reference in MPI tracer research. Since the MPI efficacy of a tracer, to our knowledge, often correlates with the tracer's performance as an MRI agent, we also analyze the nanoparticles' NMR relaxivities. Furthermore, the particles' physicochemi-

cal and magnetic properties are investigated in order to explain differences in the MPI and MRI efficacies.

## II. Materials and Methods

### II.I. Magnetosome Isolation

For magnetosome isolation, wild-type and mutant *Magnetospirillum gryphiswaldense* strains were grown under anoxic conditions in modified flask standard medium [4] at 25°C in a Biostat C fermenter (B. Braun Biotech International, Germany). After cell harvest by tangential flow filtration and centrifugation, magnetosome isolation was performed as previously described [5]. The resulting iron concentrations were 10.4 mM, 8.7 mM, 41.3 mM, 9.4 mM, and 22.5 mM for wild-type, mutant 1, mutant 2, mutant 3 and mutant 4, respectively. For further experiments, the magnetosome suspensions were diluted in a buffer containing 10 mM HEPES and 1 mM EDTA.

### II.II. Magnetosome Samples

In the present work five samples of bacterial magnetosomes were investigated. One of them was extracted from wild-type *Magnetospirillum gryphiswaldense* having a reported mean crystal diameter of  $35.6 \pm 13.0$  nm [6]. Furthermore, magnetosomes of four different mutant strains which form magnetite crystals of different core sizes due to deletions of genes involved in the biosynthesis of magnetosomes ( $\Delta F3D$  [7],  $\Delta mms48$  [6] termed mutant 1 and 4, respectively) or iron uptake systems ( $\Delta Fe4$  [8],  $\Delta feoAB1$  termed mutant 2 and 3, respectively) were used.

### II.III. Nanoparticle Characterization

The physicochemical and morphological properties of the extracted magnetosomes were analyzed by determination of the mean intensity-weighted hydrodynamic diameter via dynamic light scattering (DLS, using a NICOMP Submicron Particle Sizer Model 370, NICOMP Particle Sizing Systems) and the core size via transmission electron microscopy (TEM, using a Zeiss CEM 902 A).

To give an indication of the MPI efficacy, the Magnetic Particle Spectrum (MPS) was recorded at a drive field with an amplitude of 10 mT and a frequency of  $f_0 = 25$  kHz using a commercial magnetic particle spectrometer system (Bruker BioSpin). A minispec mq40 (Bruker BioSpin, Germany) operating at 0.94 T was used for the determination of the R1- and R2-relaxivities, which are a measure of the contrast enhancement in MRI. The effective magnetic core sizes were estimated via static magnetization measurements using an MPMS XL (Quantum Design). MPS and static magnetization curves were recorded at iron concentrations of 2.1 mM,

1.7 mM, 8.3 mM, 1.9 mM, 4.5 mM, and 5.0 mM for wild-type, mutant 1, mutant 2, mutant 3, mutant 4, and Resovist, respectively. For relaxivity measurements the relaxation times of all samples were determined at iron concentrations of 1.5 mM, 1.0 mM, 0.5 mM, and 0.1 mM.

## III. Results

### III.I. Physicochemical Characterization

Fig. 1 depicts a typical TEM micrograph of isolated wild-type magnetosomes revealing well-distributed particles and the absence of any larger particle aggregates. However, a large proportion of particles, especially the larger ones, seem to be aligned in chains, which is possibly due to magnetic interactions.

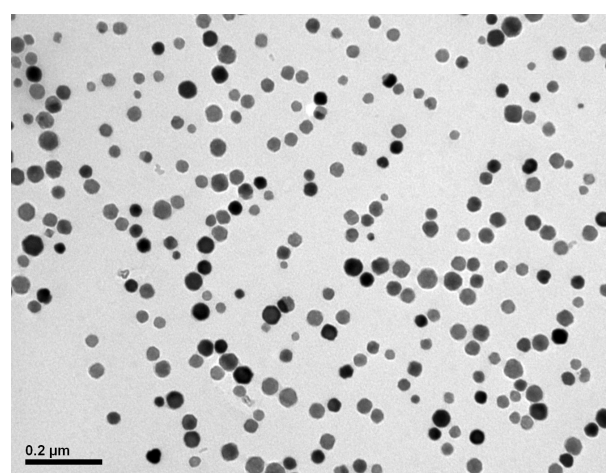


**Figure 1:** Typical TEM micrograph of extracted wild-type magnetosomes.

Typical TEM micrographs of mutant 1, 2, 3, and 4 are shown in Fig. 2. The respective crystal sizes determined from TEM are given in Tab. 1. The wild-type magnetosomes exhibit a mean crystal diameter of 36.5 nm, which is in perfect agreement with the value reported in literature [6].

The mutants 1, 2, and 3 exhibit significantly smaller crystal diameters compared to the wild-type, where the smallest mean size at 23.0 nm is observed for mutant 1.

This sample simultaneously exhibits the narrowest particle size distribution of all samples investigated here. Mutant 4, on the other hand, exhibits a larger mean particle diameter of 44.2 nm. In the respective TEM micrographs only a small amount of the particles are isolated, while most of them are connected to others, forming long chains and agglomerates.

The larger mean crystal diameters of the wild-type and mutant 4 magnetosomes are above the threshold size for superparamagnetism for cubic magnetite particles [9].

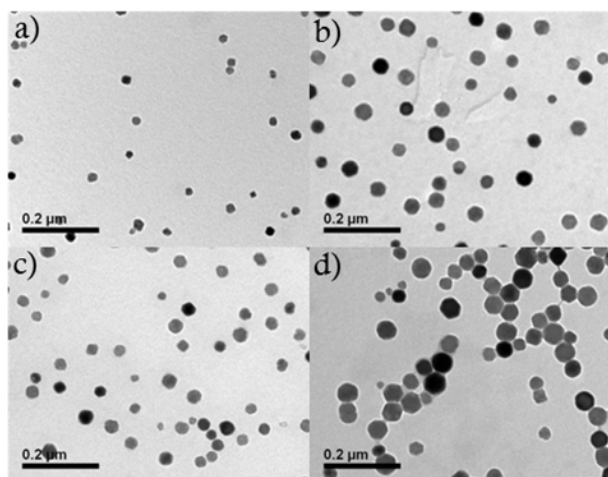


**Figure 2:** Typical TEM micrograph of isolated magnetosomes of mutant 1 (a), mutant 2 (b), mutant 3 (c), and mutant 4 (d) at identical magnifications.

Thus, a significant proportion of the particles are probably magnetically blocked at room temperature which is the reason for the formation of particle chains due to magnetic interactions. For the samples with smaller crystal diameters almost no particle chains could be observed in TEM indicating a superparamagnetic behavior.

**Table 1:** Mean crystal sizes  $d_c$  with standard deviation  $\sigma_c$  (via TEM) and mean intensity-weighted hydrodynamic diameter  $d_H$  with standard deviation  $\sigma_H$  (via DLS) of extracted magnetosomes.

Sample	$d_c^*$ [nm]	$\sigma_c^*$ [nm]	$d_H$ [nm]	$\sigma_H$ [nm]
Wild type	36.5	8.4	103	66
Mutant 1	23.0	4.0	68	35
Mutant 2	30.9	6.0	111	57
Mutant 3	32.0	6.1	96	58
Mutant 4	44.2	10.5	143	94

\* For the statistic evaluation the following number of particles was analyzed: wild-type  $n = 455$ ; mutant 1  $n = 354$ ; mutant 2  $n = 148$ ; mutant 3  $n = 366$ ; mutant 4  $n = 470$ .

DLS was used to determine the hydrodynamic diameter and the presence of particle aggregates in suspension (see Tab. 1). The wild-type magnetosomes exhibit a mean hydrodynamic diameter of  $103 \pm 66$  nm, while the diameters of the mutants vary between 68 nm and 143 nm. As expected, the hydrodynamic diameter increases with increasing crystal size; however, the former is about thrice as high. This disparity is likely to be caused through the presence of particle agglomerates and chains, which were also observed in TEM images. Note, that DLS weights those structures strongly, i.e. the signal intensity scales with the square of the volume.

### III.II. MPS and MRI efficacy

The MPS of the bacterial magnetosomes as well as of Resovist are shown in Fig. 3.

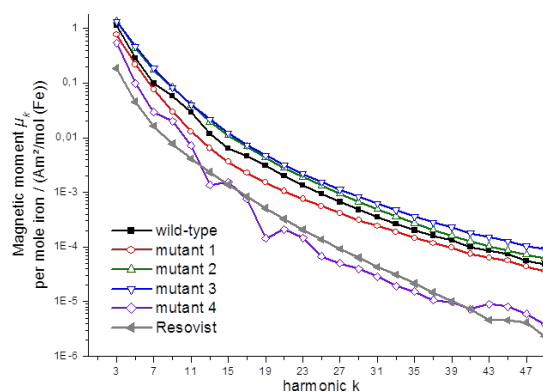


**Figure 3:** MPS of magnetosomes and Resovist measured at 10 mT and  $f_0 = 25$  kHz.

Here, mutants 2 and 3, having a mean crystal size very close to the theoretically predicted ideal size for MPI of 30 nm [10], exhibit the highest amplitudes over the entire frequency range. In contrast, the wild-type magnetosomes as well as mutant 1, having a larger and smaller diameter, respectively, exhibit a slightly lower MPS efficacy, where that of the smaller mutant 1 particles is even lower than that of the larger wild-type particles.

This correlation between core size and MPI efficacy is additionally depicted in Fig. 4 showing the ratios of the third harmonic amplitude  $\mu_3$  to the third harmonic amplitude of Resovist as a function of the crystal diameter. Here,  $\mu_3$  of all magnetosome samples exceed the amplitude of the reference Resovist by a factor of 2.9 up to 7.2 demonstrating the vast potential of bacterial magnetosomes in MPI tracer research.

Furthermore, the spectra of the wild-type magnetosomes and mutants 1, 2, and 3 exhibit a less steep slope compared to Resovist, resulting in an even more pronounced difference in the signal intensity in the higher harmonics range. However, mutant 4, which exhibits the lowest signal of the investigated samples, provides an MPS having a wave-like character, which might result from interparticle magnetic interactions due to the large particle size.

The immobilization of particles via freeze-drying results in the suppression of Brownian rotation. As a consequence the relaxation of the magnetic moments can only occur via the Néel process, e.g. the internal moments' rotation. Thus, the ratio of  $\mu_3$  of the freeze-dried sample to  $\mu_3$  of the suspended sample, where the magnetic re-orientation can additionally occur via Brownian rotation, gives an insight in the particle dynamics. As shown in Fig. 4, where the signal loss of the third harmonic am-

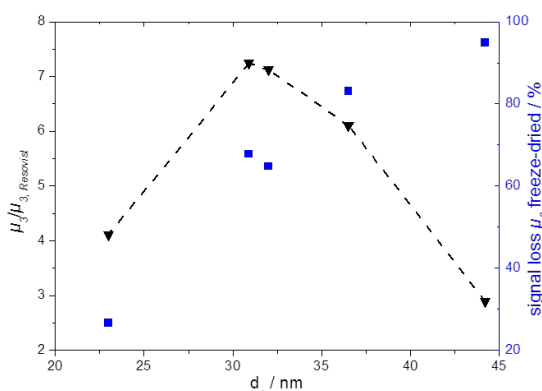


**Figure 4:** Ratios of the third harmonic amplitude  $\mu_3$  to the third harmonic amplitude of Resovist and signal loss of  $\mu_3$  upon freeze-drying as functions of crystal diameter  $d_c$ .

plitude upon freeze-drying as a function of the crystal diameter is depicted,  $\mu_3$  decreased by 27 %–95 %. Here, the sample with the smallest crystal diameter (mutant 1) exhibits the smallest signal decrease, indicating that in this sample the largest proportion of magnetic moments relax via the Néel process. With increasing crystal diameter, the signal loss due to immobilization also increases, which is in agreement with the fact, that the proportion of magnetic moments relaxing via the Néel process decreases with increasing particle core volume. Thus, the immobilization of mutant 4, exhibiting the largest core size, led to an almost complete signal loss of 95 %. For comparison, Tab. 2 shows the NMR relaxivities of the magnetosomes and Resovist determined at 0.94 T. Due to the transversal relaxivity of 219 l/(mmol·s), Resovist is often used in T2-weighted MRI sequences leading to a signal extinction of neighboring protons and thus a dark image contrast of particle-containing tissue [11]. Both the wild-type magnetosomes and all mutants exhibit higher R2 relaxivities indicative of an enhanced signal extinction in T2-weighted MRI and thus an improved imaging performance compared to the reference material. While the R2 relaxivities of mutants 1 and 4 are only slightly enhanced, the respective values of mutants 2 and the wild-type magnetosomes are more than twice as high. However, the highest R2 relaxivity of 594 l/(mmol·s) is observed for mutant 3. Thus, similar to the MPS results, magnetosomes with a crystal size around 31 nm feature the best performance in NMR relaxivity measurements. Both smaller (mutant 1) and larger (mutant 4) particles exhibited a less enhanced transversal relaxivity compared to the reference.

Furthermore, no irreversible aggregation effects, verified by DLS, could be observed after the particles were exposed to the magnetic field of 0.94 T. This indicates that the aggregation effects observed for mutant 4 in the

**Table 2:** R1- and R2 relaxivities and ratio R2/R1 of magnetosomes determined at 0.94 T and 39 °C.

Sample	R1 [l/(mmol·s)]	R2 [l/(mmol·s)]	R1/R1
Wild type	10.3	457	44.4
Mutant 1	10.9	287	26.3
Mutant 2	10.2	517	50.7
Mutant 3	12.5	594	47.5
Mutant 4	6.9	302	43.9
Resovist	20.0	219	11.0

MPS measurements, in which a significant weaker field of 10 mT was applied, are possibly due to a reversible field-induced formation of particle chains as described by Chantrell et al. [12]. This is confirmed by the fact that in the immobilized state, in which chain formation can be precluded [13], the wave-like behavior of the MPS is absent (data not shown).

### III.III. Static Magnetization

The static magnetization curves, which are shown in Fig. 5 (inset), exhibit a saturation magnetization of nearly 480 kA/m, which is the value of bulk-magnetite, indicating the purity of the crystalline phase.

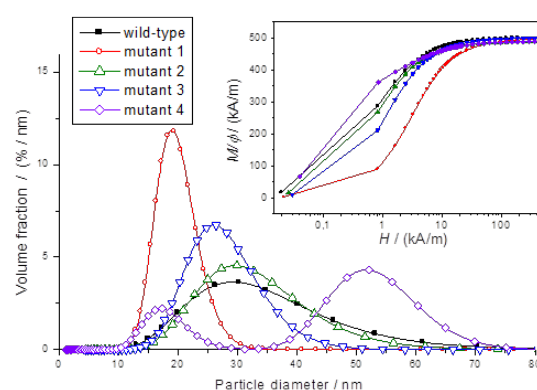


**Figure 5:** Distributions of the effective magnetic diameters of all magnetosome samples calculated from their static magnetization curves normalized to the volume fraction of magnetite (inset) using the Moment Superposition Model.

By applying the Moment Superposition Model, assuming a lognormal distribution of non-interacting magnetic moments, the mean magnetic volumes were calculated [14]. According to the best fit, a bimodal size distribution was applied for mutant 4, whereas for mutant 1–3 and the wild-type sample, a monomodal distribution fits well to the data. The size distributions are shown in Fig. 5.

Due to the different weighting of the various methods (DLS, TEM, M(H)) a comparison of the absolute effective

diameters is rather complicated. However, because of the assumption of a lognormal distribution the analysis of the M(H)-data can also yield the mean magnetic diameter  $d_m$ , which is number-weighted and thus comparable with that of TEM. The respective values are shown in Tab. 3.

**Table 3:** Mean magnetic diameters with volume fractions in brackets calculated from the static magnetization curves.

Sample	$d_c$ [nm]	$\sigma_c$ [nm]
Wild type	23.4±0.9	8.5
Mutant 1	18.1±0.1	3.2
Mutant 2	26.2±0.4	7.5
Mutant 3	24.1±0.2	5.4
Mutant 4	16.0±0.2 (20 %)	3.3
	50.0±2.0 (80 %)	7.1

For mutants 1–3, exhibiting a rather narrow size distribution,  $d_m/d_c \approx 0.8$ . This reduced effective magnetic size might be attributed to the formation of clusters during the M(H) measurement, which leads to flux closure reducing their magnetic moment. In the wild-type magnetosomes and mutant 4, where the calculated (number-weighted) mean diameter amounts only to 20 nm, this effect is even stronger. Hence, we believe that the small  $d_m/d_c$  ratios of 0.66 and 0.45 obtained for wild-type and mutant 4, respectively, are related to a high degree of dipolar interaction. This is in agreement with the large core sizes, leading to the presence of particles, which are likely no longer superparamagnetic, i.e. the magnetic moments are blocked. Furthermore, the occurrence of the bimodality in the magnetic size distribution of mutant 4 might be attributed to the increased presence of aggregates. Note that the trends in size and in the narrowness of the size distributions amongst the different samples are the same for TEM and M(H) related distributions.

## IV. Conclusion

In this work, the potentials of biogenic iron oxide nanoparticles extracted from wild-type magnetotactic bacteria of the strain *Magnetospirillum gryphiswaldense* and four mutants thereof as new tracer materials for MPI and contrast agents for MRI were analyzed and their structural and magnetic properties were investigated.

The isolated wild-type magnetosomes exhibited mean crystal diameters of 36.5 nm and the mutants diameters of 23.0 nm to 44.2 nm. The larger crystallites interact magnetically leading to the formation of chains and agglomerates, which is likely due to the loss of superparamagnetism. The MPS performances of all magnetosome samples, except mutant 4 showing strong magnetic interactions due to the large particle size, exceed the per-

formance of Resovist by far, revealing the great potential in MPI tracer research. Also in MRI the magnetosomes' contrast efficacy is superior compared to the former iron oxide-based gold-standard Resovist. However, similar to the MPS results the MRI efficacy of the sample with the largest crystal size is only slightly enhanced.

## Acknowledgements

This work was supported by DFG Priority Program 1681 (grant TR408/8) and DFG SCHU 1080/15-3 to D.S.

## References

- [1] J. W. M. Bulte and M. M. J. Modo. *Design and Applications of Nanoparticles in Biomedical Imaging*. Springer International Publishing, 2017. doi:10.1007/978-3-319-42169-8.
- [2] R. Uebe and D. Schüler. Magnetosome biogenesis in magnetotactic bacteria. *Nat. Rev. Microbiol.*, 14:621–637, 2016. doi:10.1038/nrmicro.2016.99.
- [3] A. Kraupner, D. Eberbeck, D. Heinke, R. Uebe, D. Schüler, and A. Briel. Bacterial magnetosomes - nature's powerful contribution to MPI tracer research. *Nanoscale*, 9(18):5788–5793, 2017. doi:10.1039/c7nr01530e.
- [4] U. Heyen and D. Schüler. Growth and magnetosome formation by microaerophilic *Magnetospirillum* strains in an oxygen-controlled fermentor. *Appl. Microbiol. Biotechnol.*, 61(5–6):536–544, 2003. doi:10.1007/s00253-002-1219-x.
- [5] A. Lohsse, I. Kolinko, O. Raschdorf, R. Uebe, S. Borg, A. Brachmann, J. M. Plitzko, R. Müller, Y. Zhang, and D. Schüler. Overproduction of Magnetosomes by Genomic Amplification of Biosynthesis-Related Gene Clusters in a Magnetotactic Bacterium. *Appl. Microbiol. Biotechnol.*, 82(10):3032–3041, 2016. doi:10.1128/AEM.03860-15.
- [6] A. Lohsse, S. Borg, O. Raschdorf, I. Kolinko, É. Tompa, M. Pósfai, D. Faivre, J. Baumgartner, and D. Schüler. Genetic Dissection of the mamAB and mms6 Operons Reveals a Gene Set Essential for Magnetosome Biogenesis in *Magnetospirillum gryphiswaldense*. *J. Bacteriol.*, 196(14):2658–2669, 2014. doi:10.1128/JB.01716-14.
- [7] M. Kumari, M. Widdrat, É. Tompa, E. Uebe, D. Schüler, M. Pósfai, D. Faivre, and A. M. Hirt. Distinguishing magnetic particle size of iron oxide nanoparticles with first-order reversal curves. *J. Appl. Phys.*, 116:124304, 2014. doi:10.1063/1.4896481.
- [8] R. Taukulis, M. Widdrat, M. Kumari, D. Heinke, M. Rumpfer, É. Tompa, R. Uebe, A. Kraupner, A. Cebers, D. Schüler, M. Pósfai, A. M. Hirt, and D. Faivre. Magnetic iron oxide nanoparticles as MRI contrast agents - a comprehensive physical and theoretical study. *MagnetoHydrodynamics*, 51(4):721–748, 2015.
- [9] A. R. Muxworthy and W. Williams. Critical superparamagnetic/single-domain grain sizes in interacting magnetite particles: implications for magnetosome crystals. *J. R. Soc. Interface*, 6(41):1207–1212, 2009. doi:10.1098/rsif.2008.0462.
- [10] B. Gleich and J. Weizenecker. Tomographic imaging using the nonlinear response of magnetic particles. *Nature*, 435(7046):1214–1217, 2005. doi:10.1038/nature03808.
- [11] P. Reimer and T. Balzer. Ferucarbotran (Resovist): a new clinically approved RES-specific contrast agent for contrast-enhanced MRI of the liver: properties, clinical development, and applications. *Eur. Radiol.*, 13(6):1266–1276, 2003. doi:10.1007/s00330-002-1721-7.
- [12] R. W. Chantrell, A. Bradbury, J. Popplewell, and S. W. Charles. Agglomerate formation in a magnetic fluid. *J. Appl. Phys.*, 53:2742–2744, 1982. doi:10.1063/1.330953.

- [13] N. Löwa, P. Radon, O. Kosch, and F. Wiekhorst. Concentration Dependent MPI Tracer Performance. *Intern. J. Magnetic Particle Imaging*, 2(1):1601001, 2016. doi:[10.18416/ijmpi.2016.1601001](https://doi.org/10.18416/ijmpi.2016.1601001).
- [14] D. Eberbeck, F. Wiekhorst, S. Wagner, and L. Trahms. How the size distribution of magnetic nanoparticles determines their magnetic particle imaging performance. *Appl. Phys. Lett.*, 98(18):182502, 2011. doi:[10.1063/1.3586776](https://doi.org/10.1063/1.3586776).